Acta Materialia 140 (2017) 366–374

Contents lists available at ScienceDirect

Acta Materialia

journal homepage: www.elsevier.com/locate/actamat

Full length article

Phase selection rule for Al-doped CrMnFeCoNi high-entropy alloys from first-principles

Xun Sun [a], Hualei Zhang [a, *], Song Lu [b], Xiangdong Ding [a], Yunzhi Wang [a, c], Levente Vitos [b, d, e]

[a] Center of Microstructure Science, Frontier Institute of Science and Technology, State Key Laboratory for Mechanical Behavior of Materials, Xi'an Jiaotong University, Xi'an, 710049, China
[b] Applied Materials Physics, Department of Materials Science and Engineering, Royal Institute of Technology, Stockholm, SE-10044, Sweden
[c] Department of Materials Science and Engineering, The Ohio State University, 2041 College Road, Columbus, OH 43210, USA
[d] Division of Materials Theory, Department of Physics and Materials Science, Uppsala University, P.O. Box 516, SE-75120 Uppsala, Sweden
[e] Research Institute for Solid State Physics and Optics, Wigner Research Center for Physics, Budapest H-1525, P.O. Box 49, Hungary

ARTICLE INFO

Article history:
Received 7 December 2016
Received in revised form
13 August 2017
Accepted 22 August 2017
Available online 24 August 2017

Keywords:
High-entropy alloys
Phase stability
Ab initio calculation

ABSTRACT

Using *ab initio* alloy theory, we investigate the lattice stability of paramagnetic $Al_xCrMnFeCoNi$ ($0 \leq x \leq 5$) high-entropy alloys considering the competing body-centered cubic (bcc) and face-centered cubic (fcc) crystal structures. The theoretical lattice constants increase with increasing x, in good agreement with experimental data. Upon Al addition, the crystal structure changes from fcc to bcc with a broad two-phase field region, in line with observations. The magnetic transition temperature for the bcc structure strongly decreases with x, whereas that for the fcc structure shows weak composition dependence. Within their own stability fields, both structures are predicted to be paramagnetic at ambient conditions. Bain path calculations support that within the duplex region both phases are dynamically stable. As compared to $Al_xCrFeCoNi$, equiatomic Mn addition is found to shrink the stability range of the fcc phase and delay the appearance of the bcc phase in terms of Al content, thus favoring the duplex region in 3*d*-metals based high-entropy alloys.

1. Introduction

High-entropy alloys (HEAs), originally proposed by Yeh et al. [1,2] and Cantor et al. [3,4], represent a special group of solid solutions containing five or more principal elements. As compared to the conventional one major element based alloys such as Fe-based steels or Ni-based superalloys, HEAs open a new path for developing and designing novel alloys [5–16]. These multicomponent concentrated solid solutions have been found to possess interesting and tunable properties such as high hardness, strength, toughness, ductility, oxidation and wear resistance, magnetism, superconducting, superplasticity, etc. Due to these outstanding properties, HEAs offer potential applications in many fields [1,2].

Many HEAs have been found to form single phase solid solutions within certain temperature range rather than complex structures with intermetallic compounds and multi-phases. For example, the equiatomic CrMnFeCoNi [3,17], CrFeCoNi [18], and CrCoNi [19,20], non-equiatomic $(FeNiCrMn)_{1-x}Co_x$ (x = 0.05, 0.1, and 0.2) [21], $CoNiFeAl_{0.3}Cu_{0.7}$ [22] and $AlLiMg_{0.5}ScTi_{1.5}$ [23] favor a face-centered cubic (fcc) phase, while the equiatomic NbMoTaW and VNbMoTaW [24,25], TiZrNbHfTa [26], ZrNbHfTa [27], and AlTiVNbZr [28] crystalize in a body-centered cubic (bcc) structure. Besides the large entropy of mixing, the sluggish diffusion in HEAs even at elevated temperatures enhances the metastability of solid solution phase [1,2]. The current understanding of the phase selection criteria in HEAs is based on intensive results obtained in several former studies [29–36].

The equiatomic CrMnFeCoNi alloy is often regarded as a model HEA. In contrast to the CrFeCoNi quaternary alloy, the five component CrMnFeCoNi system has larger configurational entropy and falls into the original definition of HEAs. The mechanical properties and microstructure evolutions of the equiatomic [3,17,37–57] and non-equiatomic [21,58–60] CrMnFeCoNi alloys have been measured and characterized. Cantor et al. reported that equiatomic CrMnFeCoNi forms a single fcc solid solution [3]. Gludovatz et al. found that the equiatomic CrMnFeCoNi has

* Corresponding author.
E-mail address: hualei@xjtu.edu.cn (H. Zhang).

http://dx.doi.org/10.1016/j.actamat.2017.08.045
1359-6454/

outstanding damage tolerance with tensile strengths above 1 GPa and fracture toughness values exceeding 200 MPa·$m^{1/2}$ even at a cryogenic temperature of 77 K [17,37,38]. Okamoto et al. observed that the equiatomic CrMnFeCoNi possesses ~33–43 MPa critical resolved shear stress at room temperature [39]. The microstructural evolution of the equiatomic fcc CrMnFeCoNi was evaluated after 500-day anneals at 500–900 °C and the microstructural was characterized using complementary techniques [52]. The magnitude of the average atomic displacements in the equiatomic fcc CrMnFeCoNi measured by synchrotron X-ray diffraction and determined by first-principles calculations [53], indicates that the root-mean-square atomic displacement is a valuable scaling factor to predict solid solution strengthening. An assessment of the level of local lattice strain in the equiatomic fcc CrMnFeCoNi has been studied through neutron scattering measurements [54]. The results reported by Owen et al. [54] do not confirm the presence of large local lattice strains in CrMnFeCoNi HEA. The equiatomic fcc CrMnFeCoNi alloy prepared by mechanical alloying and high-pressure sintering possesses high hardness and typical paramagnetism [56]. By tailoring the magnetic hysteresis loops of MnFeCoNiX (X = Al, Cr, Ga, and Sn) HEAs at room temperature, it was observed that the Al-, Ga-, and Sn-doped systems resemble the typical ferromagnetic (FM) behavior, while CrMnFeCoNi follows the paramagnetic (PM) behavior [61]. CrMnFeCoNi was found to have lower yield strength than CrFeCoNi possibly because Mn weakens solid solution hardening [57]. The influence of additional elements on CrMnFeCoNi has also been investigated [3,62–65]. In particular, the effect of Al on the structural and tensile properties of CrMnFeCoNi system was carefully scrutinized [62], indicating that there is a structural phase transition from fcc to bcc with increasing Al content. Similar structural transition has been found in Al_xCrCoFeNi ($0 \leq x \leq 2$) both by experimental [66–68] and theoretical [69] studies. It turned out that unlike the conventional Fe-based alloys [70–73], the effect of alloying becomes more complex and decisive in designing novel HEAs with desired properties due to the inherent multicomponent nature.

On the theoretical side, the understanding of the phase stability, mechanical and magnetic properties of the CrMnFeCoNi-based HEAs is very limited [46,74–76]. The primary goal of the present study is to reduce this gap by providing a consistent description of the fundamental properties of Al-doped CrMnFeCoNi alloys. There are a few simulations on the microstructure and mechanical properties of HEAs using conventional *ab initio* calculations [69,74,77–80]. It is found that at room temperature CrMnFeCoNi has PM fcc state [74]. Using *ab initio* magnetic exchange interactions in combination with Heisenberg model and Monte-Carlo simulations, Huang et al. demonstrated that the Curie temperature (T_C) of CrFeCoNi-based alloys is far below room-temperature in the fcc phase but increases when the bcc phase appears [81,82]. Hence, when keeping additional alloying elements at low levels and aiming at room-temperature or above, the CrFeCoNi-based alloys should be treated in the PM state.

According to the previous theoretical and experimental observations, small amount of Al doping in 3*d*-HEAs plays an important role in forming stable bcc and fcc phases or a duplex state where the two cubic phases coexist [62,83–86]. Recently, Tian et al. [69] used alloy theory to describe the phase stability of Al_xCrFeCoNi ($0 \leq x \leq 2$). They reported that the system adopts fcc structure for $x < 0.597$ and bcc structure for $x > 1.229$. In terms of valence electron concentration (VEC), these theoretical limits correspond to VEC > 7.57 and VEC < 7.04, respectively, which are in close agreement with the experimentally established phase selection rules. To the best of our knowledge, no similar theoretical limits have been established so far for the Al_xCrMnFeCoNi alloys. Adding equiatomic Mn to CrFeCoNi decreases the VEC from 8.25 to 8. Hence, one may assume that the theoretical stability fields of fcc and bcc phases should also be altered by Mn addition. Specifically, if the phase selection rule remains valid for Al_xCrMnFeCoNi, then one would expect that less Al content is required to destabilize the fcc structure and stabilize the bcc structure as compared to that in Al_xCrFeCoNi. The second goal of this work is to provide an answer to this question by systematically comparing the structural stability of paramagnetic Al_xCrMnFeCoNi alloys to that reported for Al_xCrFeCoNi.

2. Theoretical methodology

All *ab initio* calculations were performed by employing the exact muffin-tin orbitals (EMTO) method [87], based on density functional theory [88,89] and the full charge-density technique [87]. The self-consistent and total energy calculations were carried out within the Perdew-Burke-Ernzerhof (PBE) generalized gradient approximation [90] for the exchange-correlation functional. The substitutional and magnetic disorders were treated within the coherent-potential approximation (CPA) [91–94]. The PM state of Al_xCrMnFeCoNi alloys was modelled by the disordered local magnetic moment (DLM) approach [95]. In addition to the PM study, which forms the main part of this work, we also carried out calculations for the collinear magnetic (CM) configurations allowing for non-zero total magnetic moment in the system. The CM results were used to estimate the magnetic transition temperature as a function of chemical composition.

CPA is a single-site mean-field approximation. Using this approach, one completely ignores the atomic short range order and local lattice relaxation effects. Accordingly, all systems here were treated as ideal solid solutions with rigid underlying crystal structure to generate the coherent Green's function and the alloy component Green's functions (impurity Green's functions) were computed by solving the single site Dyson equation in the real space. This approach is rather standard in alloy community and has been employed in many former publications [69,72,87,93,96]. The local environment in the equiatomic fcc CrMnFeCoNi HEA has been observed by Owen et al. [54]. Comparing their results to the lattice strain for Ni powder, three NiCr binary alloys and one NiCoCr ternary alloy, indicates the absence of the severe lattice distortion as anticipated in the case of multi-component solid solutions. Based on this recent finding, the employed mean-field method is expected to have the ability to properly describe the bcc and fcc Al_xCrMnFeCoNi ($0 \leq x \leq 5$) alloys. We should also mention the appearance of phase decomposition in high Al alloys (such as the B2 phase formation) observed in experiments [62]. Since for low and intermediate Al levels (for x up to 1.5–2.0), the system is expected to form solid solution at room-temperature [97] and since most of the interesting phenomena take place within this compositional interval, here we neglect the phase decomposition and consider ideal solid solutions for all Al concentrations.

The one-electron equations were solved within the scalar-relativistic approximation and soft-core scheme. The Green's function was calculated for 16 complex energy points distributed exponentially on a semicircular contour containing the valence states below the Fermi level. In the basis set, we included *s*, *p*, *d*, and *f* orbitals ($l_{max} = 3$), and in the one-center expansion of the full charge density $l_{max} = 8$ was used. The electrostatic correction to the single-site CPA was described using the screened impurity model [98] with screening parameter 0.6. The Brillouin zones were sampled with 20 000–25 000 uniformly distributed *k*-points, which ensured the necessary convergence for all energies and energy differences. The equilibrium volume was extracted from the equation of state obtained by fitting the total energies calculated for nine different volumes by a Morse type of function [99].

3. Results

3.1. Equilibrium volume and lattice stability

We use the Wigner-Seitz radius to quantify the volume and to be able to directly compare the volumes of the two cubic lattices. In Fig. 1, we present the theoretical equilibrium Wigner-Seitz radii (w, in Bohr) and structural energy difference (ΔE, in mRy) for PM bcc and fcc $Al_xCrMnFeCoNi$ ($0 \le x \le 5$) alloys as a function of Al content. For comparison, the available experimental data for the fcc and bcc phases are also shown [62]. In general, the agreement between the present theoretical and the experimental data is satisfactory. The theoretical results slightly underestimate the Wigner-Seitz radii, which is likely to be due to the neglected thermal effects and also to the employed PBE approach. However, the observed concentration dependence of the lattice parameters for $Al_xCrMnFeCoNi$ is well captured by theory. Pure Al has larger equilibrium volume than the present host alloy, and thus its addition to CrMnFeCoNi causes a dilation of the lattice. Both theory and experiment yield positive slopes for $w(x)$ with Al addition. At low Al content, theory predicts a nearly linear variation of $\Delta w(x)/\Delta x$ ~0.028 (0.052) Bohr/x in the bcc (fcc) lattice, compared to the experimental change of ~0.025 (0.075) Bohr/x in the bcc (fcc) phase, correspondingly. Although at $x = 0$, the fcc lattice has smaller volume than the bcc one, the different composition dependences lead to $w_{fcc} > w_{bcc}$ for $x > 1.4$. The difference between the slopes of $w_{fcc}(x)$ and $w_{bcc}(x)$ might be due to the larger flexibility of the bcc structure to incorporate a large substitutional element than the close-packed fcc lattice. We recall that the number of nearest neighbor atoms increases from eight to twelve as we go from bcc to fcc lattice, which is likely to affect the flexibility to accommodate a large impurity on a lattice site.

Qualitatively the present trends for the Wigner-Seitz radii are similar to those calculated for $Al_xCrFeCoNi$ [69]. The main difference is that the crossing point between w_{fcc} and w_{bcc} occurs at $x \approx 1.8$ in Mn-free HEA [69] compared to $x \approx 1.4$ obtained for the present system. These atomic fractions correspond approximately to 31 at.% (atomic percent) and 22 at.% Al concentrations, respectively. Since the differences between the bcc and fcc equilibrium volumes of CrFeCoNi (see Ref. [69]) and CrMnFeCoNi are nearly the same, we conclude that the volume-enhancing effect of Al is different in Mn-containing and Mn-free HEAs. Namely, in $Al_xCrFeCoNi$ [69] w_{fcc} and w_{bcc} are increased by 0.047 Bohr and 0.033 Bohr, respectively, as x increases from 0 to 1. Both of these slopes are slightly larger than those obtained for the present fcc and bcc alloys: the relative changes of w_{fcc} and w_{bcc} in $Al_xCrMnFeCoNi$ are 0.045 Bohr and 0.028 Bohr as x rises from 0 to 1, respectively. Nevertheless, the difference between the fcc and bcc slopes is larger for the Mn-free alloys (0.014 Bohr) than for the Mn-containing alloys (0.017 Bohr) which explains the shift in the critical x where the two lattices have similar volumes per atom.

The theoretical structural energy difference $\Delta E(x) = E_{bcc}(x) - E_{fcc}(x)$ is shown in Fig. 1 as a function of Al content. The Al-free PM solid solution crystallizes in the fcc structure with $\Delta E(x) = 3.79$ mRy. The fcc lattice has lower energy than the bcc one for $x < 1.10$, while the bcc structure becomes stable at larger x values. For comparison, in $Al_xCrFeCoNi$ the fcc structure is stable for $x < 1.11$ [69]. The energy difference decreases with increasing x and reaches minimum value near $x \approx 2.7$. Most interestingly, close to the highest Al-content considered here, the two solid solutions have energies very close to each other suggesting the re-stabilization of the fcc lattice at very high Al-contents. Hence, the clearly bcc stabilizing effect of Al in low-Al hosts gradually changes and in high-Al hosts Al turns into an fcc stabilizer. We will return to this question below when discussing the phase stability.

3.2. Magnetic structure and magnetic transition temperature

The present PM alloys are described using a static DLM picture. Accordingly, the total magnetic moment is zero but there are non-vanishing local magnetic moments on alloy components. The theoretical local magnetic moments of $Al_xCrMnFeCoNi$ ($0 \le x \le 5$) alloys for fcc and bcc structures are plotted in Fig. 2 as a function of Al content. All moments are computed at the corresponding theoretical equilibrium volumes (see Fig. 1). The local magnetic

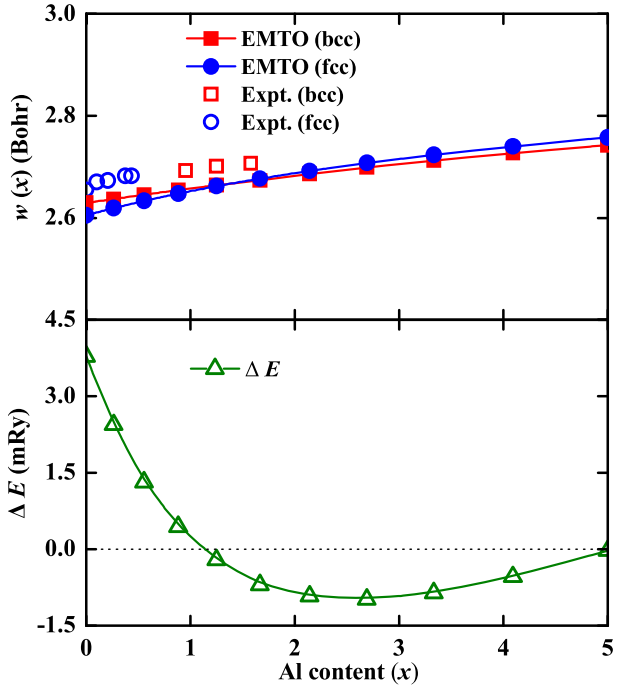

Fig. 1. Theoretical (solid symbols connected with lines) and experimental [62] (open symbols) equilibrium Wigner-Seitz radii (w, in Bohr) (upper panel) and structural energy difference (ΔE, in mRy) (lower panel) for paramagnetic bcc and fcc $Al_xCrMnFeCoNi$ ($0 \le x \le 5$) alloys as a function of Al content.

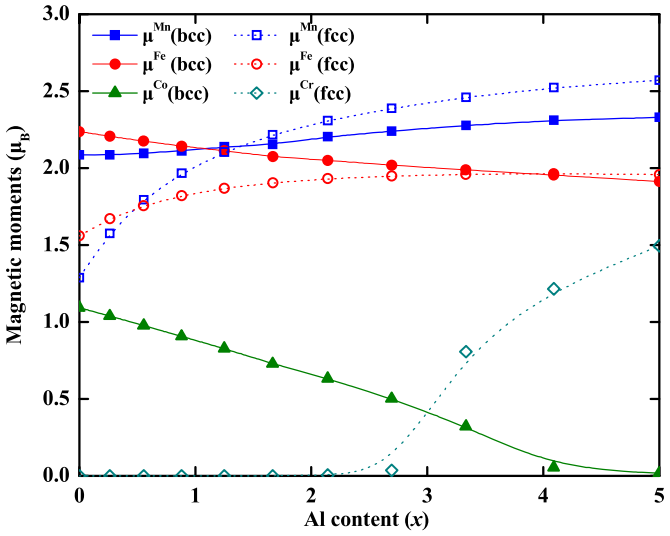

Fig. 2. Theoretical local magnetic moments at 0 K for paramagnetic bcc (solid symbols connected with lines) and fcc (open symbols connected with lines) $Al_xCrMnFeCoNi$ ($0 \le x \le 5$) alloys as a function of Al content.

moments are nonzero on the Mn, Fe, and Co (Mn, Fe, and Cr) sites in the PM bcc (fcc) structure. Previous findings claimed that Mn and Cr favor antiferromagnetic alignment with the other alloying elements in MnFeCoNi and CrMnFeCoNi [61], $AlCo_xCr_{1-x}FeNi$ alloy ($0 \le x \le 1$) [85], $Al_xCrFeNi_2Cu$ ($0 < x < 1.5$) [100], and CrFeCoNi-based HEAs [101]. We emphasize that the present results correspond to DLM picture, meaning that we mimic a totally random magnetic state rather than a collinear approximation to the PM state like in Ref. [61].

We find that μ^{Fe}(bcc) [μ^{Co}(bcc)] decreases from 2.24 (1.09) to 2.05 (0.66) μ_B as x increases from 0 to 2. On the other hand, μ^{Fe}(fcc) changes from 1.56 to 1.92 μ_B when x rises from 0 to 2. For comparison, in bcc (fcc) $Al_xCrFeCoNi$ alloys (Ref. [69]) only the Fe and Co (Fe) sites have nonzero local magnetic moments. That is, the presence of Mn induces local magnetic moments on Cr atoms in the fcc structure of the high-Al alloys. In Mn-free case (Ref. [69]), μ^{Fe}(bcc) [μ^{Co}(bcc)] decreases from 2.29 (1.13) to 2.08 (0.63) μ_B when x increases from 0 to 2, while μ^{Fe}(fcc) increases from 1.79 to 1.96 μ_B when x changes from 0 to 2. Thus, the increase of μ^{Fe}(fcc) in the Mn-containing alloys (0.36 μ_B) is almost twice as large as that in the Mn-free system (0.17 μ_B) upon adding 29 at. % Al ($x = 2$) to the host alloy. Increasing x from 0 to 2 produces slightly smaller changes in μ^{Fe}(bcc) [μ^{Co}(bcc)] in $Al_xCrMnFeCoNi$ than in $Al_xCrFeCoNi$. Based on the different magnetic moments in the Mn-containing $Al_xCrMnFeCoNi$ and Mn-free $Al_xCrFeCoNi$ systems, we conclude that the constituent elements play a crucial role in the magnetic properties of HEAs. Such findings agree well with the previous experimental measurement [56].

The μ^{Mn}(bcc) [μ^{Mn}(fcc)] in the present alloys increase from 2.09 (1.29) to 2.33 (2.57) μ_B as going from $x = 0$ to $x = 5$. The individual increments of μ^{Mn}(bcc) and μ^{Mn}(fcc) are 0.24 μ_B and 1.28 μ_B, respectively. Consequently, μ^{Mn}(bcc) slightly increases as a function of x, while the μ^{Mn}(fcc) rapidly (weakly) increases at low (high) x. Additionally, we find that μ^{Fe}(bcc) and μ^{Mn}(bcc) are larger than μ^{Fe}(fcc) and μ^{Mn}(fcc) at low x. With increasing x, due to the different composition dependences, μ^{Mn}(fcc) becomes larger than μ^{Mn}(bcc) for $x > 1.4$, while μ^{Fe}(fcc) > μ^{Fe}(bcc) for $x > 4.0$. Compared to μ^{Fe}(bcc), μ^{Fe}(fcc), μ^{Mn}(bcc), and μ^{Mn}(fcc), we find that μ^{Co}(bcc) and μ^{Cr}(PM, fcc) are relatively small and vanish around $x = 5$ and $x < 2.1$, respectively. In particular, μ^{Cr}(fcc) is almost zero for $x < 2.8$ but increases sharply above.

Recently, Huang et al. proved that Mn-free $Al_xCrFeCoNi$ HEAs in the bcc phase possesses higher Curie temperature (T_C) than in the fcc phase [81]. For example, the calculated T_C of $Al_{0.5}CrFeCoNi$ in the bcc phase is about twice of that in the fcc phase. Here we calculate T_C in the Mn-containing $Al_xCrMnFeCoNi$ HEAs. We employ the mean-field approximation, which was found to provide relatively accurate estimates for the critical temperature in HEAs [74]. Accordingly, $T_C = 2/3 \times (E^{PM}\text{-}E^{CM})/[k_B \times (1\text{-}y)]$, where E^{PM} and E^{CM} are the total energies obtained at the individual equilibrium volume for PM and CM state, respectively, and y is the concentration for the non-magnetic (Al) component, where $y = x/(5 + x)$. In our CM calculations, we find that Mn and Cr have antiparallel spin alignment relative to the other alloy constituents, which was reported also by previous studies [61,85,100,101]. We plot the theoretical Curie temperatures for the bcc (T_C^{bcc}) and fcc (T_C^{fcc}) crystal structures as a function of Al content in Fig. 3. We find that the critical temperature is larger in the bcc phase than in the fcc phase. On the other hand, T_C^{bcc} decreases quickly with increasing Al content, while T_C^{fcc} weakly decreases below $x \approx 4.09$ and increase beyond. The overall trends for both critical temperatures are similar to those reported for the Mn-free $Al_xCrFeCoNi$ HEAs [81].

For all concentrations considered here, T_C^{fcc} is far below the room-temperature and thus the fcc structure should be treated as

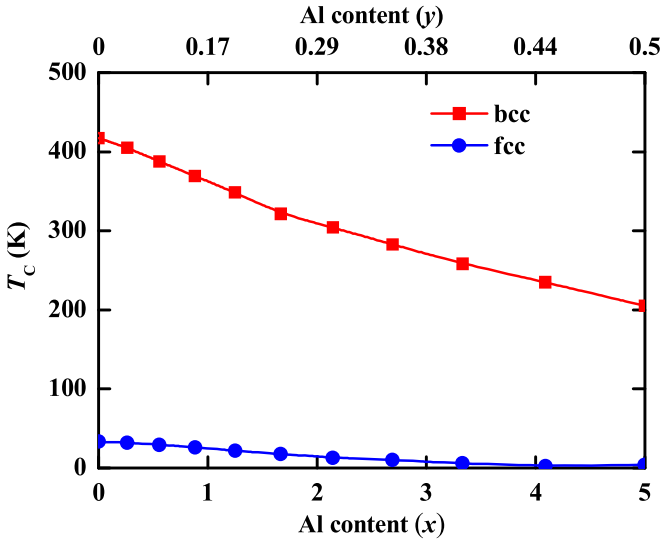

Fig. 3. Theoretical Curie temperature for bcc (solid squares connected with lines) and fcc (solid circles connected with lines) $Al_xCrMnFeCoNi$ ($0 \le x \le 5$) alloys as a function of Al content. Note that $y = x/(5 + x)$, where x is the atomic fraction of Al in $Al_xCrMnFeCoNi$ alloys.

PM. For $x < 1.1$, T_C^{bcc} is above and for $x > 1.1$ T_C^{bcc} below the room-temperature. We recall that $x \approx 1.1$ separates the two phases according to Fig. 1. This finding supports our assumption that when modeling the $Al_xCrMnFeCoNi$ system at ambient conditions one should consider the PM state. Nevertheless, due to the broad two-phase region discussed in the next section, the small fraction of bcc structure appearing in the fcc-rich duplex $Al_xCrMnFeCoNi$ HEA might still show spontaneous magnetization at room-temperature if they lose Al due to the concentration gradients. In the rest of the present work we omit this effect, assuming that it has minor impact on the phase stability. At the same time, we invite experimentalists to verify this interesting phenomenon by detecting possible magnetic bcc grains embedded in PM fcc HEA matrix.

3.3. Phase stability

We study the thermodynamics of $Al_xCrMnFeCoNi$ ($0 \le x \le 5$) system following the technique adopted by Tian et al. [69]. We approximate the $Al_xCrMnFeCoNi$ alloy with a pseudobinary system formed between Al and the host CrMnFeCoNi HEA. That is, we consider Al_yM_{1-y} with M = CrMnFeCoNi and compute the Gibbs energy as a function of $y = x/(5 + x)$. For phase α (denoting fcc or bcc), the Gibbs energy is computed relative to pure fcc CrMnFeCoNi and fcc $Al_5CrMnFeCoNi$ ($y = 0.5$) having Gibbs energies per atom $G^{fcc}(0)$ and $G^{fcc}(0.5)$, respectively, *i.e.*,

$$\Delta G^{\alpha}(y) = G^{\alpha}(y) - (1 - 2y)G^{fcc}(0) - 2yG^{fcc}(0.5).$$

Here $G^{\alpha}(y)$ is the Gibbs energy per atom for $Al_y(CrMnFeCoNi)_{1-y}$ in the α phase. We notice that the choice of the standards states has no influence on the phase stability but makes the comparison between the two competing phases easier. The individual Gibbs energies are approximated as $G^{\alpha}(y) \approx E^{\alpha}(y) - TS_{mix}(y) - TS^{\alpha}{}_{mag}(y)$, where $E^{\alpha}(y)$ is the total energy per atom for $Al_y(CrMnFeCoNi)_{1-y}$ in the α phase, and T is the temperature. The mixing entropy $S_{mix} = -k_B\sum_{i=1}^{6} c_i \ln c_i$ and the magnetic entropy $S_{mag} = k_B\sum_{i=1}^{6} C_i \ln(1 + \mu_i)$ are estimated within the mean-field approximation, where c_i is the concentration and μ_i the local

magnetic moment of the *i*th alloying element. The concentrations are $c_M = (1\text{-}y)/5$ for M = Cr, Mn, Fe, Co and Ni and $c_{Al} = y$ for Al. For each temperature, the common tangent method is used to find the stability fields of fcc and bcc phases. The total energy calculations were carried out at the theoretical equilibrium volumes.

Fig. 4 displays the fcc and bcc relative Gibbs energies for $Al_xCrMnFeCoNi$ alloys. Results are shown for four temperatures: 0, 300, 600, and 1000 K. At 0 K, the two Gibbs energies cross each other around $y = 0.183$ ($x = 1.124$) (see also Fig. 1). Below $y = 0.089$ ($x = 0.488$) the fcc phase is stable and above $y = 0.249$ ($x = 1.658$) the bcc phase is stabilized. For $0.089 < y < 0.249$ ($0.488 < x < 1.658$) both fcc and bcc phases are present. At 300 K, there is a single fcc phase for $y < 0.088$ ($x < 0.482$) and a single bcc phase for $y > 0.214$ ($x > 1.361$). The trend is similar at higher temperatures, suggesting that the duplex (fcc + bcc) region is reduced with increasing temperature especially in the bcc side of the phase diagram. In other words, temperature seems to favor the bcc lattice against the fcc one. This may be understood if we consider that the main temperature effect included in the present study is given by the magnetic entropy term and that the local magnetic moments are larger in the bcc phase than in the fcc phase for x values up to ~2.5 (y ~0.33) (see Fig. 2).

It has been suggested that the valence electron concentration (VEC) parameter qualitatively predicts the fcc/bcc phase stability in HEAs [102]. The VEC of the $Al_xCrMnFeCoNi$ system is shown in Fig. 4 (top axis). We find that at 300 K, the system prefers single fcc phase for VEC > 7.56 and single bcc phase for VEC < 6.93. For intermediate VEC values (6.93 < VEC < 7.56) the two phases co-exist. This duplex region corresponds to $0.482 < x < 1.361$. The present finding agrees quite well with the empirical VEC criterion, namely, the fcc (bcc) solid solution is stable when VEC ≥ 8.0 (VEC < 6.87) [102].

To explicitly present the temperature dependence of the phase boundaries for $Al_xCrMnFeCoNi$, we plot the individual phase limits at 0, 300, 600, and 1000 K in Fig. 5. For comparison, we also include the available experimental limits for $Al_xCrMnFeCoNi$ [62] and the theoretical phase boundaries for $Al_xCrFeCoNi$ system [69]. As shown in Fig. 5, both bcc and fcc phase boundaries for

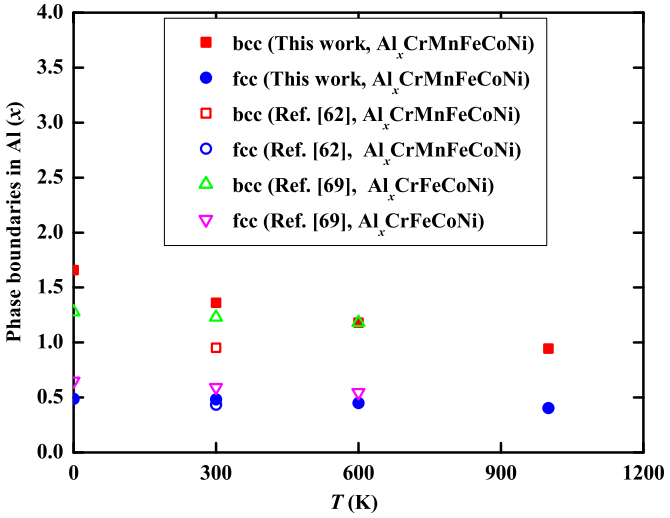

Fig. 5. Theoretical bcc (solid squares) and fcc (solid circles) phase boundaries for $Al_xCrMnFeCoNi$ ($0 \le x \le 5$) alloys as a function of temperature. Here the phase boundaries are expressed in terms of atomic fractions of Al (x). The available experimental limits for the bcc (open square) and fcc (open circle) phases for $Al_xCrMnFeCoNi$ [62] and the theoretical phase boundaries for $Al_xCrFeCoNi$ [69] are shown for comparison.

$Al_xCrMnFeCoNi$ move towards lower-Al levels, but the changes are relatively small. In the following, we compare the present theoretical fcc and bcc stability fields with those reported for Mn-free alloys [69]. This comparison is especially important since it can reveal the effect of equiatomic alloying with Mn and the robustness of the phase selection rule when going from a 5-component system to a 6-component system. The phase boundaries obtained at 0 K are shown in Table 1, and below we discuss the results at 300 K. We recall that in $Al_xCrFeCoNi$, at 300 K the formation of fcc and bcc phases appears for $x < 0.597$ and $x > 1.229$, respectively. With the VEC values, the above limits are VEC > 7.57 and VEC < 7.04,

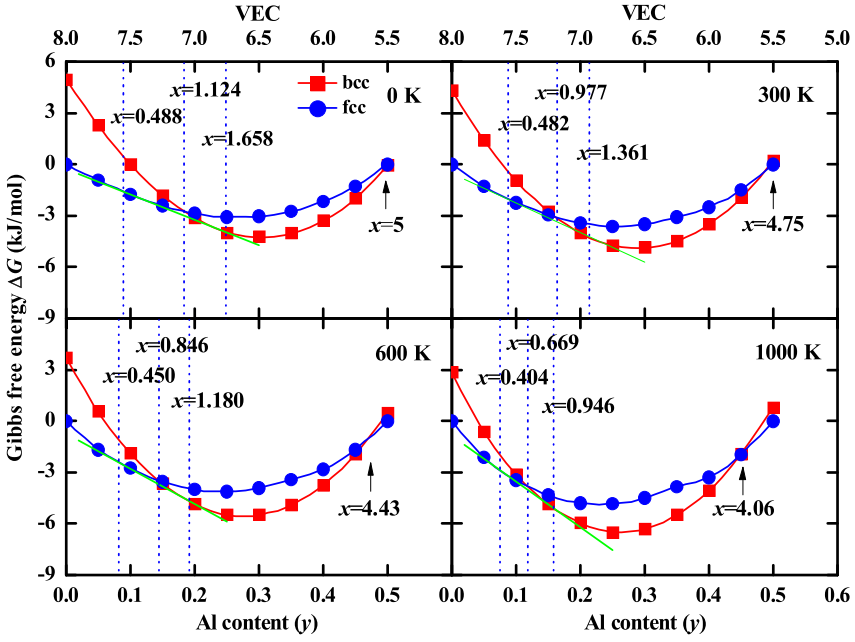

Fig. 4. Comparison of the Gibbs free energies of paramagnetic bcc (solid squares connected with lines) and fcc (solid circles connected with lines) $Al_y(CrMnFeCoNi)_{1-y}$ ($0 \le y \le 0.5$) alloys at different temperatures (T = 0, 300, 600, and 1000 K) as a function of Al content (bottom axis) and valence electron concentration (VEC) (top axis). Note that $y = x/(5 + x)$, where x is the atomic fraction of Al in $Al_xCrMnFeCoNi$ alloys.

Table 1
Theoretical fcc and bcc phase boundaries at 0 K (static conditions) for $Al_xCrFeCoNi$ (Ref. [69]) and $Al_xCrMnFeCoNi$ (present results) HEAs, along with available experimental data for $Al_xCrMnFeCoNi$ [62]. Shown are the upper and lower limits for the fcc and bcc phases expressed in terms of atomic fractions of Al (x), Al concentrations (c_{Al} in at.%) and valence electron concentration (VEC). The last four columns list the relative differences (Δ^1 in %) between the phase boundaries obtained for $Al_xCrFeCoNi$ (Ref. [69]) and $Al_xCrMnFeCoNi$ (present results) HEAs, as well as the relative phase boundaries differences (Δ^2 in %) between the present theoretical and experimental results for $Al_xCrMnFeCoNi$ HEAs [62].

	$Al_xCrFeCoNi$ (Ref. [69])		$Al_xCrMnFeCoNi$ (This work)		$Al_xCrMnFeCoNi$ (Ref. [62])		Δ^1 (%)		Δ^2 (%)	
	fcc	bcc	fcc	bcc	fcc	bcc	Δ^{fcc}	Δ^{bcc}	Δ^{fcc}	Δ^{bcc}
x	0.651	1.277	0.488	1.658	0.435	0.952	25.0	29.8	12.2	74.2
c_{Al}	14.0	24.2	8.9	24.9	8.0	16.0	36.4	2.9	11.3	55.6
VEC	7.52	6.98	7.56	6.75	7.60	7.20	0.5	3.3	0.5	6.3

respectively [69]. The comparison between the results obtained for the two alloy systems may be done on different levels. Considering first the Al fraction (x) relative to the principal elements, we find that the two-phase duplex region in the Mn-containing $Al_xCrMnFeCoNi$ system ($0.482 < x < 1.361$) is slightly wider than in the Mn-free $Al_xCrFeCoNi$ system ($0.597 < x < 1.229$). The phase stability may also be quantified in terms of concentrations. Considering the Al concentration ($c_{Al} = y$), we observe that in $Al_y(CrMnFeCoNi)_{1-y}$ less Al is enough to destabilize the fcc ($c_{Al} = 8.8$ at.%) and to stabilize the bcc ($c_{Al} = 21.4$ at.%) phase than in $Al_y(CrFeCoNi)_{1-y}$ ($c_{Al} = 13.0$ at.% and $c_{Al} = 23.5$ at.%, respectively). That is, when equiatomic Mn is present in the HEA, 8.8 at.% Al doping is sufficient to enter the duplex region as compared to 13.0 at.% needed in Mn-free case. On the other hand, stabilizing the bcc phase requires 2.1 at.% more Al in Mn-free alloy than in Mn-bearing alloy. Finally, when expressing the phase stability in terms of VEC, the variation of the duplex region upon Mn addition is calculated to be surprisingly small. Namely, the two-phase field changes from 7.04 < VEC <7.57 to 6.93 < VEC < 7.56 upon adding equiatomic Mn to $Al_xCrFeCoNi$. Similar conclusion is reached from the 0 K results (Table 1). This finding gives a theoretical confirmation for the VEC-based phase selection criterion. We should however point out that this conclusion is reached based on paramagnetic calculations for totally random solid solutions and can fail whenever a magnetic transition or a phase separation/segregation occurs.

For the Mn-bearing $Al_xCrMnFeCoNi$ HEAs, both the present theoretical results and the available experimental observation [62] indicate that a structural phase transition appears with increasing Al content. At 300 K, we find that $Al_xCrMnFeCoNi$ favors single fcc phase for $c_{Al} < 8.8$ at.% and single bcc phase for $c_{Al} > 21.4$ at.%, while a duplex fcc-bcc region corresponds to 8.8 at.% < c_{Al} < 21.4 at.%. Such phase transition is consistent with the experimental findings [62]. Namely, $Al_xCrMnFeCoNi$ alloys in the as-cast state were measured and divided into three regions: the single fcc alloys with $c_{Al} < 8$ at.% and the single bcc region with $c_{Al} > 16$ at.%, while the duplex phases with 8 at.% < c_{Al} < 16 at.%, respectively. Microstructural characterizations suggest that $Al_xCrMnFeCoNi$ ($c_{Al} > 16$ at.%) alloys consist of disordered bcc and ordered bcc (B2) phases [62]. Furthermore, it is found that the content of ordered bcc (B2) phase increases with increasing Al content [62]. In the present theoretical study, we observe a sizable difference (~33.8%) between the theoretical and the experimental phase boundaries for the bcc phase, while the difference is only ~10% for the fcc phase. Such difference between the theoretical and experimental phase boundary for the bcc structure should partly be due to the presence of the above mentioned ordered B2 structure or the short range order effects associated with the B2 formation (above the ordering temperature). Similar observation has been reported in other Al-containing HEA systems, such as AlCrFeCoNiCu [103], $Al_xCoCrFeMo_{0.5}Ni$ [104], $Al_xCrFeCoNi$ [105]. When using the theoretical phase boundaries at 0 K (Table 1), the relative differences further increase for the bcc phase but remain almost unchanged for the fcc phase. In addition to the B2 phase formation, we also associate the differences between the theoretical and experimental phase boundaries to the increased magnetic transition temperature in the bcc phase relative to that of fcc phase. In order to account for this effect one should carry out proper thermodynamic modeling of the fcc and bcc/B2 phases close to their magnetic transition temperatures. Considering the phase separation and magnetic transition effects in addition to the paramagnetic solid solutions is in progress.

Before ending this section, we briefly return and discuss the high-Al end of our theoretical phase stability study. At 0 K, $x = 5$ leads to vanishing Gibbs energy difference between the fcc and bcc phases. Increasing temperature slightly reduces this critical concentration and the fcc phase is stabilized in high-Al alloys. The fact that in high-Al alloys ($x > 2.5$) the effect of Al on the structural energy difference changes trend is in line with the theory of lattice stability of transition metals [106]. The reason for Al being fcc stabilizer in high-Al alloys but bcc stabilizer in low-Al alloys is connected to the change of the mean number of d-electrons in the system. Aluminum addition decreases the number of d electrons and thus when present in low amounts it brings the alloy closer to the bcc "deep" in the structural energy difference map [106]. On the other hand, when VEC is reduced below ~6, further Al addition brings the system away from the bcc "deep" and thus destabilizes the bcc structure. Eventually, according to the above electronic structure mechanism, in high-Al alloys the hexagonal close packed phase (not considered here) is expected to appear rather than the fcc phase.

3.4. Bain path calculations

In the previous section, we reported our phase stability study for $Al_xCrMnFeCoNi$ and demonstrated the presence of a wide two-phase region at intermediate Al concentrations. Al addition to the base CrMnFeCoNi alloy induces structural transition like in CrFeCoNi [69] and the phase boundaries (single fcc or bcc phase) of these two alloy systems are consistent with each other when expressed in terms of VEC. The thermodynamic stability is a necessary but not sufficient condition for the phase stability. One should also consider the dynamical stability. Such dynamical stability assumes that all phonon frequencies should be real. Unfortunately, today it is very cumbersome to perform full phonon calculation for multicomponent systems especially in the paramagnetic state. An alternative way to verify the mechanical stability is to consider the elastic stability criteria which can be estimated from the single-crystal elastic constants. For cubic systems, the mechanical stability requires $B = (C_{11} + 2C_{12})/3 > 0$, $C_{44} > 0$ and $C' = (C_{11}\text{-}C_{12})/2 > 0$. For the present alloys, the calculated bulk moduli are always positive, and the C_{44} values are large for both crystal structures (between 120 and 200 GPa). However, the tetragonal elastic constants C' turn out to be small (below 50 GPa)

and sensitive to the alloy composition. Here instead of discussing the alloying effects on the elastic constants, we focus on the tetragonal Bain path connecting the two cubic phases. We recall that the curvature of the potential energy surface against tetragonal lattice constant c/a is proportional to the tetragonal shear modulus C'. That is, a local minimum (the relative energy minimum along the Bain path) on the tetragonal Bain path indicates elastically (dynamically) stable lattice.

In Fig. 6, the total energies of PM $Al_xCrMnFeCoNi$ ($0 \le x \le 5$) alloys are plotted as a function of Wigner-Seitz radius w and tetragonality parameter c/a. Results are shown for eight compositions ($x = 0$, 0.26, 0.56, 1.0, 1.25, 2.14, 3.33, 5.0). The considered intervals for the Wigner-Seitz radius is $2.50 \le w/\text{Bohr} \le 2.90$ and for the tetragonal lattice parameter $0.8 \le c/a \le 1.65$.

We observe that for the Al-free alloy, there is only one minimum which corresponds to the fcc lattice ($c/a = 1.414$). This agrees well with the experimental finding that the fcc structure is the ground state of CrMnFeCoNi [17]. Upon Al addition, a second local minimum develops at $c/a = 1.0$ which corresponds to the bcc lattice. Tian et al. [69] found that two local minima exist and the ΔE between them is 0.23 mRy in AlCrFeCoNi alloy: one for bcc phase at $c/a = 1.0$ and the other for fcc $c/a = 1.414$. For the present system, the structural energy difference ΔE between the two cubic lattices gradually decreases from 3.79 mRy at $x = 0$ to 0.20 mRy at $x = 1.0$. For larger x values, the bcc lattice becomes the stable phase. These trends seen in the energy maps (Fig. 6) agree with those of the Gibbs energy (Fig. 2). The mechanical stability of the bcc lattice first increases until $x \approx 2.14$ and then decreases with further increasing x. However, both cubic lattices remain mechanically stable in terms of the tetragonal lattice distortion up to the highest Al content considered here. It is important to observe that the two elastically stable lattices possess different contour maps around the local minima (except for $x = 1$, 1.25, and 5), suggesting a sizable phonon contribution to the phase stability. Taking into account such terms requires full phonon calculations, which however are beyond the reach of today's *ab initio* methods when it comes to six component paramagnetic alloys.

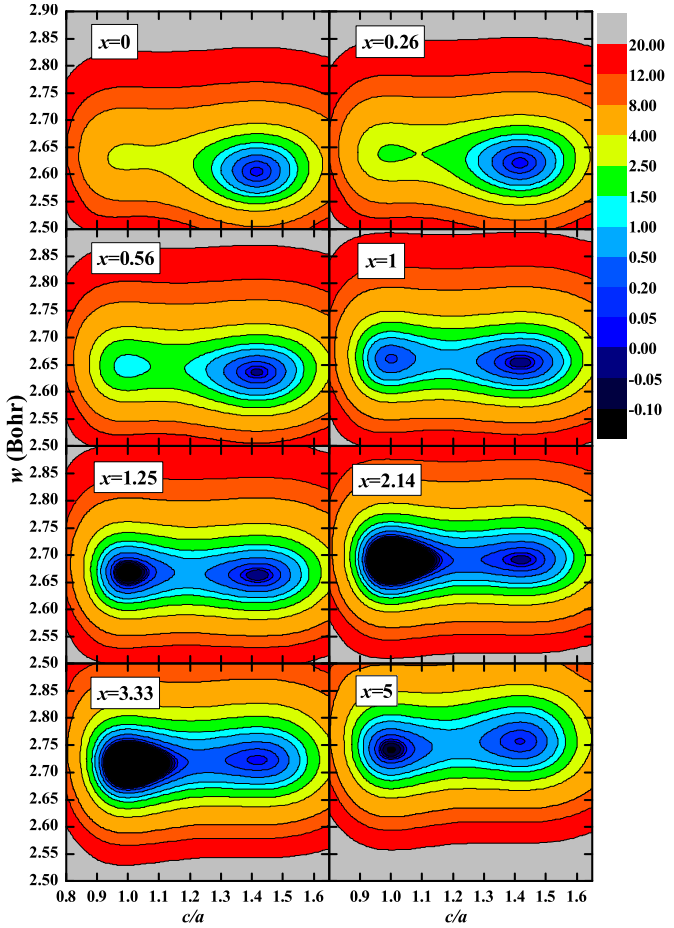

Fig. 6. Total energy contour maps (in mRy) for paramagnetic $Al_xCrMnFeCoNi$ ($0 \le x \le 5$) alloys as a function of tetragonal lattice parameter (c/a) and Wigner-Seitz radius (w in Bohr). All energies are plotted relative to the corresponding fcc ($c/a = 1.414$) minima. Maps are shown for $x = 0$, 0.26, 0.56, 1.0, 1.25, 2.14, 3.33, and 5.0.

4. Conclusions

Using first-principles alloy theory, we have investigated the phase stability and magnetic properties of paramagnetic $Al_xCrMnFeCoNi$ ($0 \le x \le 5$) high-entropy alloys considering the competing fcc and bcc crystal structures. The calculated equilibrium volumes agree well with the available experimental data for both crystals. With increasing Al content, the crystal structure of the $Al_xCrMnFeCoNi$ alloys transforms from fcc ($x < 0.482$, VEC > 7.56) to bcc ($x > 1.361$, VEC < 6.93) with a two-phase (duplex) region in between the above limits. Such phase transitions are consistent with the experimental measurements. The somewhat larger deviation between the theoretical and experimental phase boundaries in duplex-bcc zone is associated to the appearance of the B2 precipitates in the bcc phase and possible increased of the magnetic transition temperature. Further theoretical efforts are needed to resolve this question.

By comparing the phase stability boundaries for the Mn-containing $Al_xCrMnFeCoNi$ and Mn-free $Al_xCrFeCoNi$ systems, we find that Mn reduces the stability field of the fcc phase and broadens the width of the duplex region when expressed in terms of Al concentration x. When expressed in terms of valence electron concentration (VEC), it is found that the previously established phase limits are robust and show weak dependence on the base alloy composition. At 300 K, the fcc phase in the Mn-bearing (Mn-free) alloys is predicted to be stable for VEC > 7.56 (VEC > 7.57), while the bcc phase is stable for VEC < 6.93 (VEC < 7.04). The magnetic transition temperatures for both cubic phases are found to be below the room-temperature within their respective stability fields. However, magnetic bcc grains may appear in the fcc part of the two-phase region due to Al-depletion of the bcc phase.

The Bain path calculations indicate that upon Al doping, both crystal structures remain elastically stable, supporting their co-existence within the duplex region. For a more complete dynamical stability, however, one should go beyond the elastic stability and investigate the full phonon spectra as a function of composition. The present results demonstrate the ability of using *ab initio* alloy theory for studying phase stability of paramagnetic HEAs, and provide a theoretical verification for the phase selection rules based on valence electron concentration.

Acknowledgements

H. L. Zhang acknowledges helpful discussion with F. Y. Tian. The National Natural Science Foundation of China (No. 51301126), the National Basic Research Program of China (No. 2014CB644003), the National Key Research and Development Program of China (No. 2016YFB0701302), the Fundamental Research Funds for the Central Universities, the Swedish Research Council (VR), the Swedish Foundation for Strategic Research (SSF), the Swedish Foundation for International Cooperation in Research and Higher Education (STINT), the Carl Tryggers Foundations, the Swedish Governmental Agency for Innovation Systems (VINNOVA), and the Hungarian

Scientific Research Fund (research project OTKA 109570) are acknowledged for financial support. Y. W. acknowledges the financial support of NSF under Grant DMR-1534826.

References

[1] J.W. Yeh, S.K. Chen, S.J. Lin, J.Y. Gan, T.S. Chin, T.T. Shun, C.H. Tsau, S.Y. Chang, Nanostructured high-entropy alloys with multiple principal elements: novel alloy design concepts and outcomes, Adv. Eng. Mater. 6 (5) (2004) 299–303.

[2] J.W. Yeh, S.K. Chen, J.Y. Gan, S.J. Lin, T.S. Chin, T.T. Shun, C.H. Tsau, S.Y. Chang, Formation of simple crystal structures in Cu-Co-Ni-Cr-Al-Fe-Ti-V alloys with multiprincipal metallic elements, Metall. Mater. Trans. A 35A (8) (2004) 2533–2536.

[3] B. Cantor, I.T.H. Chang, P. Knight, A.J.B. Vincent, Microstructural development in equiatomic multicomponent alloys, Mater. Sci. Eng. A 375–377 (2004) 213–218.

[4] B. Cantor, Multicomponent and high entropy alloys, Entropy 16 (9) (2014) 4749.

[5] Y. Zhang, T.T. Zuo, Z. Tang, M.C. Gao, K.A. Dahmen, P.K. Liaw, Z.P. Lu, Microstructures and properties of high-entropy alloys, Prog. Mater. Sci. 61 (0) (2014) 1–93.

[6] E.J. Pickering, N.G. Jones, High-entropy alloys: a critical assessment of their founding principles and future prospects, Int. Mater. Rev. 61 (3) (2016) 183–202.

[7] M.C. Gao, D.E. Alman, Searching for next single-phase high-entropy alloy compositions, Entropy 15 (10) (2013) 4504–4519.

[8] Y.F. Ye, Q. Wang, J. Lu, C.T. Liu, Y. Yang, High-entropy alloy: challenges and prospects, Mater. Today 19 (6) (2016) 349–362.

[9] C. Zhang, F. Zhang, H. Diao, M.C. Gao, Z. Tang, J.D. Poplawsky, P.K. Liaw, Understanding phase stability of Al-Co-Cr-Fe-Ni high entropy alloys, Mater. Des. 109 (2016) 425–433.

[10] L. Liu, J.B. Zhu, L. Li, J.C. Li, Q. Jiang, Microstructure and tensile properties of $FeMnNiCuCoSn_x$ high entropy alloys, Mater. Des. 44 (0) (2013) 223–227.

[11] T. Yang, S. Xia, S. Liu, C. Wang, S. Liu, Y. Fang, Y. Zhang, J. Xue, S. Yan, Y. Wang, Precipitation behavior of AlxCoCrFeNi high entropy alloys under ion irradiation, Sci. Rep. 6 (2016) 32146.

[12] F. He, Z. Wang, Y. Li, Q. Wu, J. Li, J. Wang, C.T. Liu, Kinetic ways of tailoring phases in high entropy alloys, Sci. Rep. 6 (2016) 34628.

[13] Y. Lu, Y. Dong, S. Guo, L. Jiang, H. Kang, T. Wang, B. Wen, Z. Wang, J. Jie, Z. Cao, H. Ruan, T. Li, A promising new class of high-temperature alloys: eutectic high-entropy alloys, Sci. Rep. 4 (2014) 6200.

[14] Y. Shi, B. Yang, P. Liaw, Corrosion-Resistant high-entropy alloys: a review, Metals 7 (2) (2017) 43.

[15] D.B. Miracle, O.N. Senkov, A critical review of high entropy alloys and related concepts, Acta Mater. 122 (2017) 448–511.

[16] S. Gorsse, D.B. Miracle, O.N. Senkov, Mapping the world of complex concentrated alloys, Acta Mater. 135 (2017) 177–187.

[17] B. Gludovatz, A. Hohenwarter, D. Catoor, E.H. Chang, E.P. George, R.O. Ritchie, A fracture-resistant high-entropy alloy for cryogenic applications, Science 345 (6201) (2014) 1153–1158.

[18] M.S. Lucas, G.B. Wilks, L. Mauger, J.A. Munoz, O.N. Senkov, E. Michel, J. Horwath, S.L. Semiatin, M.B. Stone, D.L. Abernathy, E. Karapetrova, Absence of long-range chemical ordering in equimolar FeCoCrNi, Appl. Phys. Lett. 100 (25) (2012) 251907.

[19] Z. Zhang, H. Sheng, Z. Wang, B. Gludovatz, Z. Zhang, E.P. George, Q. Yu, S.X. Mao, R.O. Ritchie, Dislocation mechanisms and 3D twin architectures generate exceptional strength-ductility-toughness combination in CrCoNi medium-entropy alloy, Nat. Commun. 8 (2017) 14390.

[20] Z. Wu, H. Bei, G.M. Pharr, E.P. George, Temperature dependence of the mechanical properties of equiatomic solid solution alloys with face-centered cubic crystal structures, Acta Mater. 81 (2014) 428–441.

[21] Z.G. Zhu, K.H. Ma, X. Yang, C.H. Shek, Annealing effect on the phase stability and mechanical properties of $(FeNiCrMn)_{(100-x)}Co_x$ high entropy alloys, J. Alloy. Compd. 695 (2017) 2945–2950.

[22] Z. Fu, W. Chen, H. Wen, D. Zhang, Z. Chen, B. Zheng, Y. Zhou, E.J. Lavernia, Microstructure and strengthening mechanisms in an FCC structured single-phase nanocrystalline $Co_{25}Ni_{25}Fe_{25}Al_{7.5}Cu_{17.5}$ high-entropy alloy, Acta Mater. 107 (2016) 59–71.

[23] K.M. Youssef, A.J. Zaddach, C. Niu, D.L. Irving, C.C. Koch, A novel low-density, high-hardness, high-entropy alloy with close-packed single-phase nanocrystalline structures, Mater. Res. Lett. 3 (2) (2015) 95–99.

[24] O.N. Senkov, G.B. Wilks, J.M. Scott, D.B. Miracle, Mechanical properties of $Nb_{25}Mo_{25}Ta_{25}W_{25}$ and $V_{20}Nb_{20}Mo_{20}Ta_{20}W_{20}$ refractory high entropy alloys, Intermetallics 19 (5) (2011) 698–706.

[25] O.N. Senkov, G.B. Wilks, D.B. Miracle, C.P. Chuang, P.K. Liaw, Refractory high-entropy alloys, Intermetallics 18 (9) (2010) 1758–1765.

[26] O.N. Senkov, J.M. Scott, S.V. Senkova, D.B. Miracle, C.F. Woodward, Microstructure and room temperature properties of a high-entropy TaNbHfZrTi alloy, J. Alloy. Compd. 509 (20) (2011) 6043–6048.

[27] S. Maiti, W. Steurer, Structural-disorder and its effect on mechanical properties in single-phase TaNbHfZr high-entropy alloy, Acta Mater. 106 (2016) 87–97.

[28] B. Vishwanadh, N. Sarkar, S. Gangil, S. Singh, R. Tewari, G.K. Dey, S. Banerjee, Synthesis and microstructural characterization of a novel multicomponent equiatomic ZrNbAlTiV high entropy alloy, Scr. Mater. 124 (2016) 146–150.

[29] O.N. Senkov, D.B. Miracle, A new thermodynamic parameter to predict formation of solid solution or intermetallic phases in high entropy alloys, J. Alloy. Compd. 658 (2016) 603–607.

[30] D.J.M. King, S.C. Middleburgh, A.G. McGregor, M.B. Cortie, Predicting the formation and stability of single phase high-entropy alloys, Acta Mater. 104 (2016) 172–179.

[31] A. Takeuchi, K. Amiya, T. Wada, K. Yubuta, Alloy design for high-entropy alloys based on Pettifor map for binary compounds with 1:1 stoichiometry, Intermetallics 66 (2015) 56–66.

[32] G. Anand, R. Goodall, C.L. Freeman, Role of configurational entropy in body-centred cubic or face-centred cubic phase formation in high entropy alloys, Scr. Mater. 124 (2016) 90–94.

[33] Y.F. Ye, Q. Wang, J. Lu, C.T. Liu, Y. Yang, Design of high entropy alloys: a single-parameter thermodynamic rule, Scr. Mater. 104 (2015) 53–55.

[34] O.N. Senkov, J.D. Miller, D.B. Miracle, C. Woodward, Accelerated exploration of multi-principal element alloys with solid solution phases, Nat. Commun. 6 (2015) 6529.

[35] L.J. Santodonato, Y. Zhang, M. Feygenson, C.M. Parish, M.C. Gao, R.J.K. Weber, J.C. Neuefeind, Z. Tang, P.K. Liaw, Deviation from high-entropy configurations in the atomic distributions of a multi-principal-element alloy, Nat. Commun. 6 (2015) 5964.

[36] Z. Leong, J.S. Wróbel, S.L. Dudarev, R. Goodall, I. Todd, D. Nguyen-Manh, The effect of electronic structure on the phases present in high entropy alloys, Sci. Rep. 7 (2017) 39803.

[37] B. Gludovatz, A. Hohenwarter, K.V.S. Thurston, H. Bei, Z. Wu, E.P. George, R.O. Ritchie, Exceptional damage-tolerance of a medium-entropy alloy CrCoNi at cryogenic temperatures, Nat. Commun. 7 (2016) 10602.

[38] Z. Zhang, M.M. Mao, J. Wang, B. Gludovatz, Z. Zhang, S.X. Mao, E.P. George, Q. Yu, R.O. Ritchie, Nanoscale origins of the damage tolerance of the high-entropy alloy CrMnFeCoNi, Nat. Commun. 6 (2015) 10143.

[39] N.L. Okamoto, S. Fujimoto, Y. Kambara, M. Kawamura, Z.M.T. Chen, H. Matsunoshita, K. Tanaka, H. Inui, E.P. George, Size effect, critical resolved shear stress, stacking fault energy, and solid solution strengthening in the CrMnFeCoNi high-entropy alloy, Sci. Rep. 6 (2016) 35863.

[40] F. Otto, A. Dlouhy, C. Somsen, H. Bei, G. Eggeler, E.P. George, The influences of temperature and microstructure on the tensile properties of a CoCrFeMnNi high-entropy alloy, Acta Mater. 61 (15) (2013) 5743–5755.

[41] A. Gali, E.P. George, Tensile properties of high- and medium-entropy alloys, Intermetallics 39 (0) (2013) 74–78.

[42] F. Otto, Y. Yang, H. Bei, E.P. George, Relative effects of enthalpy and entropy on the phase stability of equiatomic high-entropy alloys, Acta Mater. 61 (7) (2013) 2628–2638.

[43] A. Haglund, M. Koehler, D. Catoor, E.P. George, V. Keppens, Polycrystalline elastic moduli of a high-entropy alloy at cryogenic temperatures, Intermetallics 58 (2015) 62–64.

[44] K.Y. Tsai, M.H. Tsai, J.W. Yeh, Sluggish diffusion in Co–Cr–Fe–Mn–Ni high-entropy alloys, Acta Mater. 61 (13) (2013) 4887–4897.

[45] G. Laplanche, P. Gadaud, O. Horst, F. Otto, G. Eggeler, E.P. George, Temperature dependencies of the elastic moduli and thermal expansion coefficient of an equiatomic, single-phase CoCrFeMnNi high-entropy alloy, J. Alloy. Compd. 623 (2015) 348–353.

[46] A.J. Zaddach, C. Niu, C.C. Koch, D.L. Irving, Mechanical properties and stacking fault energies of NiFeCrCoMn high-entropy alloy, JOM 65 (12) (2013) 1780–1789.

[47] B. Schuh, F. Mendez-Martin, B. Völker, E.P. George, H. Clemens, R. Pippan, A. Hohenwarter, Mechanical properties, microstructure and thermal stability of a nanocrystalline CoCrFeMnNi high-entropy alloy after severe plastic deformation, Acta Mater. 96 (2015) 258–268.

[48] N. Stepanov, M. Tikhonovsky, N. Yurchenko, D. Zyabkin, M. Klimova, S. Zherebtsov, A. Efimov, G. Salishchev, Effect of cryo-deformation on structure and properties of CoCrFeNiMn high-entropy alloy, Intermetallics 59 (2015) 8–17.

[49] C. Zhu, Z.P. Lu, T.G. Nieh, Incipient plasticity and dislocation nucleation of FeCoCrNiMn high-entropy alloy, Acta Mater. 61 (8) (2013) 2993–3001.

[50] W.H. Liu, Y. Wu, J.Y. He, T.G. Nieh, Z.P. Lu, Grain growth and the Hall–Petch relationship in a high-entropy FeCrNiCoMn alloy, Scr. Mater. 68 (7) (2013) 526–529.

[51] B.-R. Chen, A.-C. Yeh, J.-W. Yeh, Effect of one-step recrystallization on the grain boundary evolution of CoCrFeMnNi high entropy alloy and its subsystems, Sci. Rep. 6 (2016) 22306.

[52] F. Otto, A. Dlouhý, K.G. Pradeep, M. Kuběnová, D. Raabe, G. Eggeler, E.P. George, Decomposition of the single-phase high-entropy alloy CrMnFeCoNi after prolonged anneals at intermediate temperatures, Acta Mater. 112 (2016) 40–52.

[53] N.L. Okamoto, K. Yuge, K. Tanaka, H. Inui, E.P. George, Atomic displacement in the CrMnFeCoNi high-entropy alloy - a scaling factor to predict solid solution strengthening, AIP Adv. 6 (12) (2016) 125008.

[54] L.R. Owen, E.J. Pickering, H.Y. Playford, H.J. Stone, M.G. Tucker, N.G. Jones, An assessment of the lattice strain in the CrMnFeCoNi high-entropy alloy, Acta Mater. 122 (2017) 11–18.

[55] R. Raghavan, C. Kirchlechner, B.N. Jaya, M. Feuerbacher, G. Dehm, Mechanical size effects in a single crystalline equiatomic FeCrCoMnNi high entropy alloy, Scr. Mater. 129 (2017) 52–55.

[56] P.F. Yu, L.J. Zhang, H. Cheng, H. Zhang, M.Z. Ma, Y.C. Li, G. Li, P.K. Liaw, R.P. Liu, The high-entropy alloys with high hardness and soft magnetic property prepared by mechanical alloying and high-pressure sintering, Intermetallics 70 (2016) 82–87.

[57] S.H. Joo, H. Kato, M.J. Jang, J. Moon, C.W. Tsai, J.W. Yeh, H.S. Kim, Tensile deformation behavior and deformation twinning of an equimolar CoCrFeMnNi high-entropy alloy, Mater. Sci. Eng. A 689 (2017) 122–133.

[58] M.J. Yao, K.G. Pradeep, C.C. Tasan, D. Raabe, A novel, single phase, non-equiatomic FeMnNiCoCr high-entropy alloy with exceptional phase stability and tensile ductility, Scr. Mater. 72–73 (2014) 5–8.

[59] K.G. Pradeep, C.C. Tasan, M.J. Yao, Y. Deng, H. Springer, D. Raabe, Non-equiatomic high entropy alloys: approach towards rapid alloy screening and property-oriented design, Mater. Sci. Eng. A 648 (2015) 183–192.

[60] Z. Li, K.G. Pradeep, Y. Deng, D. Raabe, C.C. Tasan, Metastable high-entropy dual-phase alloys overcome the strength–ductility trade-off, Nature 534 (7606) (2016) 227–230.

[61] T. Zuo, M.C. Gao, L. Ouyang, X. Yang, Y. Cheng, R. Feng, S. Chen, P.K. Liaw, J.A. Hawk, Y. Zhang, Tailoring magnetic behavior of CoFeMnNiX (X = Al, Cr, Ga, and Sn) high entropy alloys by metal doping, Acta Mater. 130 (2017) 10–18.

[62] J.Y. He, W.H. Liu, H. Wang, Y. Wu, X.J. Liu, T.G. Nieh, Z.P. Lu, Effects of Al addition on structural evolution and tensile properties of the FeCoNiCrMn high-entropy alloy system, Acta Mater. 62 (2014) 105–113.

[63] I.S. Wani, G.D. Sathiaraj, M.Z. Ahmed, S.R. Reddy, P.P. Bhattacharjee, Evolution of microstructure and texture during thermo-mechanical processing of a two phase $Al_{0.5}$CoCrFeMnNi high entropy alloy, Mater. Charact. 118 (2016) 417–424.

[64] N.D. Stepanov, N.Y. Yurchenko, M.A. Tikhonovsky, G.A. Salishchev, Effect of carbon content and annealing on structure and hardness of the CoCrFeNiMn-based high entropy alloys, J. Alloy. Compd. 687 (2016) 59–71.

[65] N.D. Stepanov, D.G. Shaysultanov, R.S. Chernichenko, N.Y. Yurchenko, S.V. Zherebtsov, M.A. Tikhonovsky, G.A. Salishchev, Effect of thermo-mechanical processing on microstructure and mechanical properties of the carbon-containing CoCrFeNiMn high entropy alloy, J. Alloy. Compd. 693 (2017) 394–405.

[66] H.P. Chou, Y.S. Chang, S.K. Chen, J.W. Yeh, Microstructure, thermophysical and electrical properties in Al_xCoCrFeNi ($0 \le x \le 2$) high-entropy alloys, Mater. Sci. Eng. B 163 (3) (2009) 184–189.

[67] Y.F. Kao, T.J. Chen, S.K. Chen, J.W. Yeh, Microstructure and mechanical property of as-cast, -homogenized, and -deformed AlxCoCrFeNi ($0 \le x \le 2$) high-entropy alloys, J. Alloy. Compd. 488 (1) (2009) 57–64.

[68] W.R. Wang, W.L. Wang, S.C. Wang, Y.C. Tsai, C.H. Lai, J.W. Yeh, Effects of Al addition on the microstructure and mechanical property of Al_xCoCrFeNi high-entropy alloys, Intermetallics 26 (2012) 44–51.

[69] F.Y. Tian, L. Delczeg, N.X. Chen, L.K. Varga, J. Shen, L. Vitos, Structural stability of NiCoFeCrAlx high-entropy alloy from ab initio theory, Phys. Rev. B 88 (8) (2013) 085128.

[70] H.L. Zhang, X. Li, S. Schönecker, H. Jesperson, B. Johansson, L. Vitos, Anomalous elastic hardening in Fe-Co alloys at high temperature, Phys. Rev. B 89 (18) (2014) 184107.

[71] H.L. Zhang, M.P.J. Punkkinen, B. Johansson, L. Vitos, Elastic parameters of paramagnetic iron-based alloys from first-principles calculations, Phys. Rev. B 85 (5) (2012) 054107.

[72] H.L. Zhang, M.P.J. Punkkinen, B. Johansson, S. Hertzman, L. Vitos, Single-crystal elastic constants of ferromagnetic bcc Fe-based random alloys from first-principles theory, Phys. Rev. B 81 (18) (2010) 184105.

[73] H.L. Zhang, B. Johansson, L. Vitos, Ab initio calculations of elastic properties of bcc Fe-Mg and Fe-Cr random alloys, Phys. Rev. B 79 (22) (2009) 224201.

[74] D. Ma, B. Grabowski, F. Körmann, J. Neugebauer, D. Raabe, Ab initio thermodynamics of the CoCrFeMnNi high entropy alloy: importance of entropy contributions beyond the configurational one, Acta Mater. 100 (2015) 90–97.

[75] F. Tian, L.K. Varga, J. Shen, L. Vitos, Calculating elastic constants in high-entropy alloys using the coherent potential approximation: current issues and errors, Comput. Mater. Sci. 111 (2016) 350–358.

[76] S. Huang, W. Li, S. Lu, F. Tian, J. Shen, E. Holmström, L. Vitos, Temperature dependent stacking fault energy of FeCrCoNiMn high entropy alloy, Scr. Mater. 108 (2015) 44–47.

[77] F.Y. Tian, L.K. Varga, N.X. Chen, L. Delczeg, L. Vitos, Ab initio investigation of high-entropy alloys of 3*d* elements, Phys. Rev. B 87 (7) (2013) 075144.

[78] F. Tian, L.K. Varga, N. Chen, J. Shen, L. Vitos, Ab initio design of elastically isotropic $TiZrNbMoV_x$ high-entropy alloys, J. Alloy. Compd. 599 (0) (2014) 19–25.

[79] C. Li, M. Zhao, J.C. Li, Q. Jiang, B2 structure of high-entropy alloys with addition of Al, J. Appl. Phys. 104 (11) (2008) 113504.

[80] A. Sharma, P. Singh, D.D. Johnson, P.K. Liaw, G. Balasubramanian, Atomistic clustering-ordering and high-strain deformation of an $Al_{0.1}$CrCoFeNi high-entropy alloy, Sci. Rep. 6 (2016) 31028.

[81] S. Huang, W. Li, X. Li, S. Schönecker, L. Bergqvist, E. Holmström, L.K. Varga, L. Vitos, Mechanism of magnetic transition in FeCrCoNi-based high entropy alloys, Mater. Des. 103 (2016) 71–74.

[82] S. Huang, Á. Vida, D. Molnár, K. Kádas, L.K. Varga, E. Holmström, L. Vitos, Phase stability and magnetic behavior of FeCrCoNiGe high-entropy alloy, Appl. Phys. Lett. 107 (25) (2015) 251906.

[83] C.J. Tong, Y.L. Chen, S.K. Chen, J.W. Yeh, T.T. Shun, C.H. Tsau, S.J. Lin, S.Y. Chang, Microstructure characterization of Al_xCoCrCuFeNi high-entropy alloy system with multiprincipal elements, Metall. Mater. Trans. A 36A (4) (2005) 881–893.

[84] C.J. Tong, M.R. Chen, S.K. Chen, J.W. Yeh, T.T. Shun, S.J. Lin, S.Y. Chang, Mechanical performance of the AlxCoCrCuFeNi high-entropy alloy system with multiprincipal elements, Metall. Mater. Trans. A 36A (5) (2005) 1263–1271.

[85] T. Borkar, V. Chaudhary, B. Gwalani, D. Choudhuri, C.V. Mikler, V. Soni, T. Alam, R.V. Ramanujan, R. Banerjee, A combinatorial approach for assessing the magnetic properties of high entropy alloys: role of Cr in $AlCo_xCr_{1-x}$FeNi, Adv. Eng. Mater. (2017) 1700048.

[86] D. Choudhuri, B. Gwalani, S. Gorsse, C.V. Mikler, R.V. Ramanujan, M.A. Gibson, R. Banerjee, Change in the primary solidification phase from fcc to bcc-based B2 in high entropy or complex concentrated alloys, Scr. Mater. 127 (2017) 186–190.

[87] L. Vitos, Total-energy method based on the exact muffin-tin orbitals theory, Phys. Rev. B 64 (1) (2001) 014107.

[88] P. Hohenberg, W. Kohn, Inhomogeneous electron gas, Phys. Rev. 136 (3B) (1964) B864–B871.

[89] W. Kohn, L.J. Sham, Self-consistent equations including exchange and correlation effects, Phys. Rev. 140 (4A) (1965) A1133–A1138.

[90] J.P. Perdew, K. Burke, M. Ernzerhof, Generalized gradient approximation made simple, Phys. Rev. Lett. 77 (18) (1996) 3865–3868.

[91] P. Soven, Coherent-potential model of substitutional disordered alloys, Phys. Rev. 156 (3) (1967) 809–813.

[92] B.L. Gyorffy, Coherent-potential approximation for a nonoverlapping-muffin-tin-potential model of random substitutional alloys, Phys. Rev. B 5 (6) (1972) 2382–2384.

[93] L. Vitos, I.A. Abrikosov, B. Johansson, Anisotropic lattice distortions in random alloys from first-principles theory, Phys. Rev. Lett. 87 (15) (2001) 156401.

[94] L. Vitos, The EMTO method and applications, in: Computational Quantum Mechanicals for Materials Engineers, Springer-Verlag, London, 2007.

[95] B.L. Györffy, A.J. Pindor, G.M. Stocks, J. Staunton, H. Winter, J. Phys. F. Met. Phys. 15 (1985) 1337.

[96] L. Vitos, P.A. Korzhavyi, B. Johansson, Stainless steel optimization from quantum mechanical calculations, Nat. Mater. 2 (1) (2003) 25–28.

[97] S. Huang, W. Li, E. Holmström, L. Vitos. Unpublished.

[98] P.A. Korzhavyi, A.V. Ruban, I.A. Abrikosov, H.L. Skriver, Madelung energy for random metallic alloys in the coherent potential approximation, Phys. Rev. B 51 (9) (1995) 5773–5780.

[99] V.L. Moruzzi, J.F. Janak, K. Schwarz, Calculated thermal properties of metals, Phys. Rev. B 37 (2) (1988) 790–799.

[100] T. Borkar, B. Gwalani, D. Choudhuri, C.V. Mikler, C.J. Yannetta, X. Chen, R.V. Ramanujan, M.J. Styles, M.A. Gibson, R. Banerjee, A combinatorial assessment of Al_xCrCuFeNi$_2$ ($0 < x < 1.5$) complex concentrated alloys: microstructure, microhardness, and magnetic properties, Acta Mater. 116 (2016) 63–76.

[101] F. Körmann, D. Ma, D.D. Belyea, M.S. Lucas, C.W. Miller, B. Grabowski, M.H.F. Sluiter, "Treasure maps" for magnetic high-entropy-alloys from theory and experiment, Appl. Phys. Lett. 107 (14) (2015) 142404.

[102] S. Guo, C.T. Liu, Phase stability in high entropy alloys: formation of solid-solution phase or amorphous phase, Pro. Nat. Sci. Mater. Int. 21 (6) (2011) 433–446.

[103] Y.P. Wang, B.S. Li, H.Z. Fu, Solid solution or intermetallics in a high-entropy alloy, Adv. Eng. Mater. 11 (8) (2009) 641–644.

[104] C.-Y. Hsu, C.-C. Juan, T.-S. Sheu, S.-K. Chen, J.-W. Yeh, Effect of aluminum content on microstructure and mechanical properties of Al_xCoCrFeMo$_{0.5}$Ni high-entropy alloys, JOM 65 (12) (2013) 1840–1847.

[105] Y. Ma, B. Jiang, C. Li, Q. Wang, C. Dong, P. Liaw, F. Xu, L. Sun, The BCC/B2 morphologies in Al_xNiCoFeCr high-entropy alloys, Metals 7 (2) (2017) 57.

[106] H.L. Skriver, Crystal structure from one-electron theory, Phys. Rev. B 31 (4) (1985) 1909–1923.